Iranian Journal of Astronomy and Astrophysics
Vol. 12, No. 3, Summer 2025, 227–239
©Available online at http://ijaa.du.ac.ir
DOI: 10.22128/ijaa.2025.3144.1231
Online ISSN: 2383–403X

Iranian Journal of Astronomy and Astrophysics

Research Paperr

Analytical Study of Gravitational Magnetoacoustic Waves in the Solar Corona

Mohammadamin Zeynali Sabeg[1] · Zahra Fazel*[2]
[1] Faculty of Physics, University of Tabriz, Tabriz, Iran;
E-mail: aminzeynali594@gmail.com
[2] Faculty of Physics, University of Tabriz, Tabriz, Iran;
*E-mail: z_fazel@tabrizu.ac.ir

Received: 16 November 2025; **Accepted:** 25 December 2025; **Published:** 27 December 2025

Abstract. Coronal loops are one of the important waveguides in the solar atmosphere. Waveguides can be considered as the magnetic flux tubes for the generation and propagation of magnetohydrodynamic waves. In this paper, we have used a cylindrical geometry model to study the behavior of magnetohydrodynamic waves in coronal loops analytically. We considered a plasma structure with gravity acceleration and a uniform magnetic field. Wave equations were derived under specific assumptions and initial conditions. After linearization, perturbations were applied to obtain the dispersion relation. Using the dispersion equation, we obtained the frequency graph in terms of wave number. We investigated the effect of some parameters such as density, Alfvén velocity and gravitational acceleration on the behavior of waves. Our analysis of wave's behavior across different kL regimes, and the observed convergence of phase speeds toward specific limits, provided valuable information regarding mode stability. The results showed that the sausage and kink modes approach each other at particular values of kL, where their phase speeds act as asymptotes. This convergence behavior demonstrates a fundamental relationship between these two types of wave modes under varying waveguide thickness conditions.

Keywords: The Sun, The Solar Corona, Coronal Loops, Magnetohydrodynamic Waves, Dispersion Relation, Cylindrical Geometry.

1 Introduction

Coronal loops are arch-shaped magnetic structures filled with hot plasma. Studying the characteristics of these structures plays a vital role in understanding the solar magnetic field and plasma interactions in the corona. In particular, investigating the behavior of magnetohydrodynamic (MHD) waves in coronal loops is essential for understanding the processes responsible for heating the solar corona and accelerating the solar wind. Despite significant advancements in observational techniques and numerical simulations, the exact mechanisms of energy transport and dissipation in coronal loops remain an active area of research. One of the important applications of studying waves in the solar atmosphere is that it provides the ability to infer key physical parameters through coronal seismology. The frequent occurrence

---

* *Corresponding author*

of slow magnetoacoustic waves makes them particularly valuable for diagnosing the plasma and magnetic properties of coronal structures [1]. Among the various MHD wave modes, sausage modes ($m = 0$) are anti-symmetric, fast magnetoacoustic oscillations in coronal loops that cause periodic expansions and contractions of the loop radius without displacing the axis. These modes occur primarily in thick, dense loops and play a crucial role in coronal diagnostics as well as in understanding wave-driven heating and solar wind acceleration [2]. In contrast, kink oscillations are standing fast magnetoacoustic modes whose periods are mainly determined by the loop length, making them natural eigenmodes of the magnetic waveguide. Kink oscillations can appear in both rapidly decaying and decayless regimes, and their sensitivity to plasma and magnetic parameters makes them powerful tools for coronal seismology [3]. More generally, kink waves manifest as propagating modes in open-field regions or in large closed magnetic structures, such as extended coronal loops, while they appear as standing modes in relatively small coronal loops, present in both quiet-Sun and active regions [4].

This work focuses on the analytical study of MHD waves in coronal loops modeled using cylindrical geometry. The cylindrical model provides a simple yet insightful framework for analyzing MHD wave dynamics in such structures. The study begins with a brief overview of the Sun, emphasizing the corona and coronal loops. Then, we review the fundamental principles of magnetohydrodynamics and their application in the solar corona, followed by the modeling of a coronal loop with cylindrical geometry, considering appropriate magnetic field configurations and plasma characteristics. Subsequently, we derive the dispersion relations for MHD waves in cylindrical coordinates under ideal conditions and relevant boundary constraints. Through this analytical approach, we aim to identify key parameters that influence wave behavior, such as wave speed, frequency, and mode structure. Roberts et al investigated wave propagation in magnetically structured atmospheres [5]. Their study addressed surface wave propagation along magnetic interfaces and laid the foundation for understanding how magnetic field discontinuities affect wave behavior in coronal environments. Roberts (1981) extended this by analyzing wave propagation in an isolated magnetic slab, assuming no lateral perturbation transmission and neglecting gravity [6]. Roberts and Edwin (1982) explored wave propagation in a magnetic slab embedded in a magnetized medium [7]. Nakariakov and Roberts (1995) investigated magnetoacoustic waves in structured atmospheres with steady plasma flows, considering magnetic slab models applicable to the solar corona [8]. Noémi Kinga Zsámberger , Matthew Alcock, and Robert Erdélyi (2018) studied magnetoacoustic waves in a magnetic slab embedded in an asymmetric magnetic environment [9]. Their model extended classical symmetric slab models developed by Roberts and built upon previous work by Alcock and Erdélyi by considering a homogeneous magnetic layer between two semi-infinite plasma regions with different densities, temperatures, and magnetic field strengths. This model provides important contributions to coronal seismology. Edwin and Roberts (1983) examined wave propagation in magnetic cylinders and modeled coronal loops as homogeneous magnetic cylinders [10]. They derived dispersion relations for different MHD wave modes in cylindrical geometry, which remains a fundamental framework for the study of MHD waveguides. S. Pary, P. de Bruyne, and collaborators (1996) proposed numerical simulations of guided MHD waves in coronal loops [11]. In their work, the solar corona is modeled as a high-conductivity, low-beta plasma slab, where MHD waves are excited by the motion of coronal loop footpoints at the base of the photosphere.

2 Theoretical Model and Methodology

In this study, we aim to derive the dispersion relation of magnetohydrodynamic (MHD) waves under specific conditions by employing the single-fluid MHD equations and the linearization method.

Waves are at the heart of plasma physics. Similar to other physical media, waves in a plasma represent small oscillations that propagate through the medium. When a localized disturbance occurs at one point, it leads to oscillations at another point later in time. Thus, studying waves requires analyzing how small perturbations behave around a state of equilibrium.

In a plasma, such as that found in the solar atmosphere, there are generally four types of wave modes driven by various restoring forces. Magnetic tension and Coriolis forces can produce Alfvén and inertial waves, respectively. Magnetic pressure, plasma pressure, and gravity can independently generate fast magnetoacoustic, acoustic, and internal gravity waves. However, when these three forces act together, two distinct modes known as magnetoacoustic-gravity waves emerge. In the absence of gravity, these reduce to magnetoacoustic waves, and when the magnetic field is negligible, they become pure acoustic-gravity waves.

The standard procedure in wave dynamics starts by establishing an equilibrium configuration, then introducing small perturbations to it. The governing MHD equations are linearized to examine whether the disturbances propagate in the form of waves. The main goal is to find the dispersion relation, expressing the wave frequency ω in terms of the wavenumber k and other plasma parameters.

We use the ideal, single-fluid, non-dissipative MHD framework, under the assumptions of adiabatic processes, negligible Coriolis force, incompressibility, quasi-neutrality, and ideal fluid conditions. The basic equations governing mass continuity, momentum conservation, energy conservation, and magnetic induction are reformulated accordingly to facilitate wave analysis.

The governing MHD equations are [12]

$$\frac{\partial \mathbf{B}}{\partial t} = \nabla \times (\mathbf{v} \times \mathbf{B}), \tag{1}$$

$$\frac{d\rho}{dt} + \rho (\nabla \cdot \mathbf{v}) = 0, \tag{2}$$

$$\rho \frac{d\mathbf{v}}{dt} = -\nabla P + \mathbf{j} \times \mathbf{B} - \rho g(r)\, \hat{\mathbf{r}}, \tag{3}$$

$$p = \frac{k_B}{m} \rho T, \tag{4}$$

$$\frac{\rho^\gamma}{\gamma - 1} \frac{d}{dt} \left(\frac{p}{\rho^\gamma} \right) = -\nabla \cdot \mathbf{q} - L_r + \frac{j^2}{\sigma} + F_H, \tag{5}$$

where $\mathbf{B}$ is the magnetic field, $\mathbf{v}$ is the plasma velocity, ρ is the mass density, P is the gas pressure, and T is the temperature. The current density is $\mathbf{j} = \nabla \times \mathbf{B}/\mu_0$ with μ_0 the magnetic permeability of free space. The gravitational acceleration is $g(r)$ along $\hat{\mathbf{r}}$. Equation (4) is the ideal gas law, with k_B the Boltzmann constant and m the mean particle mass. The adiabatic index is γ. Heat flux is $\mathbf{q}$, L_r radiative losses, σ conductivity, and F_H additional heating (e.g. turbulence or waves). For local analysis, gravity is approximated as $\rho g \hat{z}$ with g constant and $\hat{z}$ vertical [12].

2.1 Geometric Configuration and Physical Assumptions

We examine MHD wave propagation in a coronal loop modeled as a cylindrical waveguide. The loop is a vertically oriented magnetic cylinder of radius L and length h, with $h \gg L$, rooted on a spherical solar surface of radius R where $R \gg L$ (see Figure 1).

Analytical solutions are sought under simplifying assumptions. We assume hydrostatic equilibrium before perturbations. The equilibrium plasma is static ($\mathbf{v}_0 = 0$), with uniform vertical magnetic field $\mathbf{B}_0 = B_0 \hat{e}_z$, uniform temperature T_0, and stratified density $\rho_0(z)$ and pressure $p_0(z)$. Small perturbations yield

$$\rho = \rho_0 + \rho_1, \qquad \rho_1 \ll \rho_0, \tag{6}$$

$$\mathbf{v} = \mathbf{v}_1, \tag{7}$$

$$p = p_0 + p_1, \qquad p_1 \ll p_0, \tag{8}$$

$$\mathbf{B} = \mathbf{B}_0 + \mathbf{B}_1, \qquad |\mathbf{B}_1| \ll |\mathbf{B}_0|. \tag{9}$$

In the presence of gravity, the equilibrium pressure and density in a coronal loop obey the hydrostatic balance equation

$$-\frac{dp_0}{dz} - \rho_0 g = 0, \tag{10}$$

where g is the gravitational acceleration. Assuming an isothermal atmosphere and the validity of the ideal gas law, the equilibrium density and pressure vary exponentially with height,

$$\rho_0(z) = \rho_0 \, \exp\left(-\frac{z}{H}\right), \qquad p_0(z) = p_0 \, \exp\left(-\frac{z}{H}\right), \tag{11}$$

where H is the density scale height, given by

$$H = \frac{k_B T}{mg} = \frac{p_0}{\rho_0 g}. \tag{12}$$

where k_B is Boltzmann's constant, T is the temperature, m is the mean mass of a particle, g is the gravitational acceleration, p_0 is the pressure at the reference level, and ρ_0 is the density at the reference level[12].

Using the typical coronal loop parameters provided in Tables 1 and 2, and adopting temperatures in the range $T = 1$–3 MK characteristic of hot X-ray emitting loops [13,14], the corresponding scale height is found to be approximately

$$H \approx 1.0 \times 10^5 \text{ km}. \tag{13}$$

Table 1: Typical parameters of X-ray coronal loops [13].

Loop type	**Length** (10^9 cm)	**Temperature** (MK)	**Density** (10^9 cm^{-3})
Bright points	0.1–1	2	5
Active region loops	1–10	3	1–10
Giant arches	10–100	1–2	0.1–1
Flare loops	1–10	>10	>50

Table 2: Morphological properties of hot coronal loops [14].

Quantity	**Value**	**Wavelength**	**Disk (d) or Limb (l)**
Height (km)	110000–130000	EUV	d
	∼45000	21 cm	d
Length (km)	18000–29000	EUV	d
	7000–44000	X-ray	d
	10000–100000	X-ray	d
	50000–500000	X-ray	d
	70000–100000	6 & 20 cm	d
Diameter (km)	3000–22000	3530 Å	l
	3000–18000	EUV new	d, l

2.1.1 Justification of the Local Uniform-Density Approximation

Although the solar corona is gravitationally stratified, with pressure and density varying on the characteristic scale height, A comparison with the observationally inferred loop heights listed in Table 2 shows that for many hot coronal loops the geometrical height is significantly smaller than the scale height ($z \ll H$). Therefore, over the vertical extent relevant to the present study, the exponential variation in Eqs. (14) remains weak. Consequently, the equilibrium density and pressure may be treated as locally uniform to an excellent approximation, which justifies neglecting their explicit z-dependence in the derivation of the dispersion relation. This approach is commonly adopted in analytical MHD wave models of coronal loops, where the gravitational acceleration is retained in the linearized equations while the background plasma parameters are approximated as locally constant. therefore

$$\rho_0(z) = \rho_0 \qquad p_0(z) = p_0 \tag{14}$$

2.2 Linearization of Perturbed MHD Equations

Substituting Eqs. (6)–(9) into the governing system (1)–(5), and neglecting quadratic perturbation terms, yields:

$$\frac{\partial \rho_1}{\partial t} + (\mathbf{v}_1 \cdot \nabla)\rho_0 + \rho_0(\nabla \cdot \mathbf{v}_1) = 0, \tag{15}$$

$$\rho_0 \frac{\partial \mathbf{v}_1}{\partial t} = -\nabla p_1 + (\nabla \times \mathbf{B}_1) \times \frac{\mathbf{B}_0}{\mu_0} - \rho_1 g \hat{\mathbf{e}}_z, \tag{16}$$

$$\frac{\partial p_1}{\partial t} + (\mathbf{v}_1 \cdot \nabla)p_0 - c_s^2 \left(\frac{\partial \rho_1}{\partial t} + (\mathbf{v}_1 \cdot \nabla)\rho_0 \right) = 0, \tag{17}$$

$$\frac{\partial \mathbf{B}_1}{\partial t} = \nabla \times (\mathbf{v}_1 \times \mathbf{B}_0), \tag{18}$$

$$\nabla \cdot \mathbf{B}_1 = 0, \tag{19}$$

where c_s is the adiabatic sound speed,

$$c_s = \sqrt{\frac{\gamma p_0}{\rho_0}} = \sqrt{\frac{\gamma k_B T_0}{m}}. \tag{20}$$

These linearized equations form the basis for deriving dispersion relations for MHD waves in cylindrical loop models.

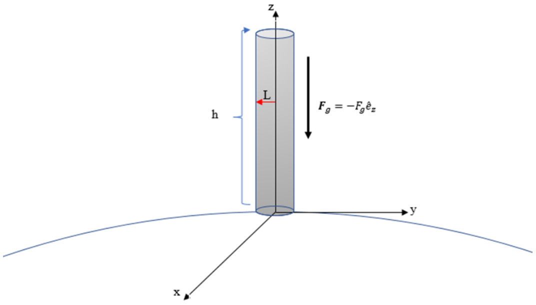

Figure 1: Schematic representation of the cylindrical model of a coronal loop. The loop is modeled as a vertical magnetic cylinder of radius L and length h, rooted on the solar surface with radius $R \gg L$.

3 Derivation of the Dispersion Relation

By taking the partial time derivative $\frac{\partial}{\partial t}$ of Eq. (16) and applying the previous relations, the general wave equation for the perturbed velocity $\mathbf{v}_1$ becomes

$$\frac{\partial^2 \mathbf{v}_1}{\partial t^2} = c_s^2 \nabla(\nabla \cdot \mathbf{v}_1) - (\gamma - 1) g\, \hat{\mathbf{e}}_z (\nabla \cdot \mathbf{v}_1) - g \nabla v_{1z} + \left\{ \nabla \times \left[\nabla \times (\mathbf{v}_1 \times \mathbf{B}_0) \right] \right\} \times \frac{\mathbf{B}_0}{\mu_0 \rho_0}. \tag{21}$$

We define the divergence of the perturbed velocity as

$$\Delta = \nabla \cdot \mathbf{v}_1 = R(r) \exp\left(i k_z z + i n \varphi - i \omega t \right). \tag{22}$$

Substituting Eq. (22) into the wave equation (21), one obtains

$$\frac{\partial^2 \mathbf{v}_1}{\partial t^2} = c_s^2 \nabla \Delta - (\gamma - 1) g\, \hat{\mathbf{e}}_z \Delta - g \nabla v_{1z} + \left\{ \nabla \times \left[\nabla \times (\mathbf{v}_1 \times \mathbf{B}_0) \right] \right\} \times \frac{\mathbf{B}_0}{\mu_0 \rho_0}. \tag{23}$$

The relation between v_{1z} and Δ is

$$\left(\frac{\partial^2}{\partial t^2} + g \frac{\partial}{\partial z} \right) v_{1z} = c_s^2 \frac{\partial \Delta}{\partial z} - (\gamma - 1) g \Delta. \tag{24}$$

Applying $\left(\frac{\partial^2}{\partial t^2} + g \frac{\partial}{\partial z} \right) \nabla$ to both sides of Eq. (23) and using Eq. (24), the following differential equation for Δ is derived

$$\begin{aligned} \left(\frac{\partial^2}{\partial t^2} + g \frac{\partial}{\partial z} \right) \frac{\partial^2 \Delta}{\partial t^2} &= (c_s^2 + v_A^2) \left(\frac{\partial^2}{\partial t^2} + g \frac{\partial}{\partial z} \right) \nabla^2 \Delta \\ &\quad - v_A^2 \nabla^2 \frac{\partial}{\partial z} \Delta - (\gamma - 1) g \left(\frac{\partial^2}{\partial t^2} + g \frac{\partial}{\partial z} \right) \Delta. \end{aligned} \tag{25}$$

Neglecting imaginary terms, the simplified form becomes

$$\frac{-\left(\omega^4 - k_z^2 g^2 \right)}{\left[-\left(c_s^2 - v_A^2 \right) \omega^2 - k_z^2 v_A^2 c_s^2 + (\gamma - 1) g^2 \right]} \Delta + \nabla^2 \Delta = 0. \tag{26}$$

The cylindrical Laplacian for Δ is

$$\nabla^2\Delta = \frac{1}{r}\frac{\partial}{\partial r}\left(r\frac{\partial\Delta}{\partial r}\right) + \left(\frac{-n^2}{r^2} - k^2\right)\Delta. \tag{27}$$

For convenience, we define $k_z \equiv k$ and $k_\varphi^2 \equiv n^2$ and introduce

$$m^2 = k^2 + \frac{\omega^4 - k^2g^2}{-(c_s^2 + v_A^2)\omega^2 + k^2v_A^2c_s^2 + (\gamma-1)g^2}. \tag{28}$$

Thus, the radial differential equation becomes

$$\frac{1}{r}\frac{d}{dr}\left(r\frac{dR}{dr}\right) - \left(\frac{n^2}{r^2} + m^2\right)R = 0. \tag{29}$$

3.1 Boundary Conditions and Dispersion Relation

The quantity m^2 is defined separately inside and outside the loop
Inside the loop ($r < L$):

$$m_i^2 = k^2 + \frac{\omega^4 - k^2g^2}{-(c_{si}^2 + v_{Ai}^2)\omega^2 + k^2v_{Ai}^2c_{si}^2 + (\gamma-1)g^2}, \tag{30}$$

Outside the loop ($r \geq L$):

$$m_e^2 = k^2 + \frac{\omega^4 - k^2g^2}{-(c_{se}^2 + v_{Ae}^2)\omega^2 + k^2v_{Ae}^2c_{se}^2 + (\gamma-1)g^2}. \tag{31}$$

Solutions: - For surface waves ($m_i^2 > 0$):

$$R(r) = R_iI_n(m_ir), \qquad r < L, \tag{32}$$

- For body waves ($m_i^2 = -n_i^2 < 0$):

$$R(r) = R_iJ_n(n_ir), \qquad r < L, \tag{33}$$

- For the external region ($r \geq L$):

$$R(r) = R_eK_n(m_er). \tag{34}$$

At the boundary $r = L$, continuity of total pressure and radial velocity leads to the dispersion relations
Surface waves:

$$\frac{\rho_i}{\rho_e}\left(\frac{k^2v_{Ai}^2 - \omega^2}{k^2v_{Ae}^2 - \omega^2}\right)\frac{m_e}{m_i} = \frac{I_n'(m_iL)K_n(m_eL)}{K_n'(m_eL)I_n(m_iL)}, \tag{35}$$

Body waves:

$$\frac{\rho_i}{\rho_e}\left(\frac{k^2v_{Ai}^2 - \omega^2}{k^2v_{Ae}^2 - \omega^2}\right)\frac{m_e}{m_i} = \frac{J_n'(n_iL)K_n(m_eL)}{K_n'(m_eL)J_n(n_iL)}. \tag{36}$$

These dispersion relations are valid under $m_e > 0$, ensuring wave amplitudes decay for $r \gg L$. Depending on n, the modes are: - $n = 0$: sausage (symmetric), - $n = 1$: kink (asymmetric), - $n > 1$: higher-order fluting modes.

3.2 Cut-off Frequencies and the Role of Gravitational acceleration

The transition between surface and body wave behavior in each region of the flux tube is determined by the sign of the radial wavenumbers m_i^2 and m_e^2. The cut-off frequencies therefore obtained from the conditions $m_i^2 = 0$ and $m_e^2 = 0$. Setting either radial wavenumber to zero leads to a quadratic equation in ω^2. Introducing $X = \omega^2$ and using the corresponding internal or external values of the sound and Alfvén speeds, the general cut-off condition can be written as

$$X^2 - k^2(c_s^2 + v_A^2)\,X + k^2\left(k^2 v_A^2 c_s^2 + (\gamma - 2)\,g^2\right) = 0. \tag{37}$$

For the internal cut-off frequency, the values of v_A and c_s are taken as v_{Ai} and c_{Si}, respectively, while for the external cut-off frequency, v_{Ae} and c_{Se} are used.
Solving Eq. (37) yields the analytical expressions for the cut-off frequencies,

$$\omega_c^2 = \frac{k^2(c_s^2 + v_A^2) \pm \sqrt{k^4(c_s^2 + v_A^2)^2 - 4k^2\left(k^2 v_A^2 c_s^2 + (\gamma - 2)g^2\right)}}{2}. \tag{38}$$

This relation defines the upper and lower cut-off branches $\omega_{c,+}(k)$ and $\omega_{c,-}(k)$. The behaviour of these solutions is shown in Fig. 2, where both internal and external cut-off curves are displayed using the physical parameters in Table 3.

The term $(\gamma - 2)g^2$ represents the influence of a uniform gravitational acceleration on the cut-off structure. For typical coronal values ($\gamma = 5/3$), this contribution is negative and slightly modifies the balance of restoring forces. Although the effect is modest for the parameter values adopted here, its influence becomes clearer at small wavenumbers. Figures 4 and 5 compare the results with and without gravity.

3.3 Gravity-free limit ($g = 0$)

Setting $g = 0$ eliminates the gravitational term from Eq. (38). and the cut-off frequencies reduce to

$$\omega_c^2 = \frac{k^2(c_s^2 + v_A^2) \pm k^2|c_s^2 - v_A^2|}{2}. \tag{39}$$

Thus,

$$\omega_{c,+}^2 = k^2 \max(c_s^2,\, v_A^2), \qquad \omega_{c,-}^2 = k^2 \min(c_s^2,\, v_A^2). \tag{40}$$

Hence, in the gravity-free limit the two cut-off branches correspond simply to the characteristic speeds of the medium: the upper branch $\omega_{c,+}$ is set by the larger of (c_s, v_A) and the lower branch $\omega_{c,-}$ by the smaller. These relations are the classical MHD cut-off frequencies for a uniform cylindrical plasma and shown in Fig. 3 using the parameters in Table 3, and they provide a convenient reference for assessing the small gravitational correction seen in Fig. 2.

4 Discussion and Conclusions

In this study, we derived the dispersion relation for magnetohydrodynamic (MHD) waves in cylindrical waveguides, modeling solar coronal loops as ideal plasmas under appropriate boundary and continuity conditions. By plotting the normalized phase speed c_{phase}/v_{Ai} as a function of kL, and using the gravitational acceleration in the corona ($g = 274\ \mathrm{m\,s^{-2}}$) together with the physical parameter listed in Table 3 (see also Fig. 6), we investigated the effects of density contrast, relative Alfvén speeds, and sound speed ratios, as well as the influence of gravitational acceleration, on wave propagation and mode behavior.

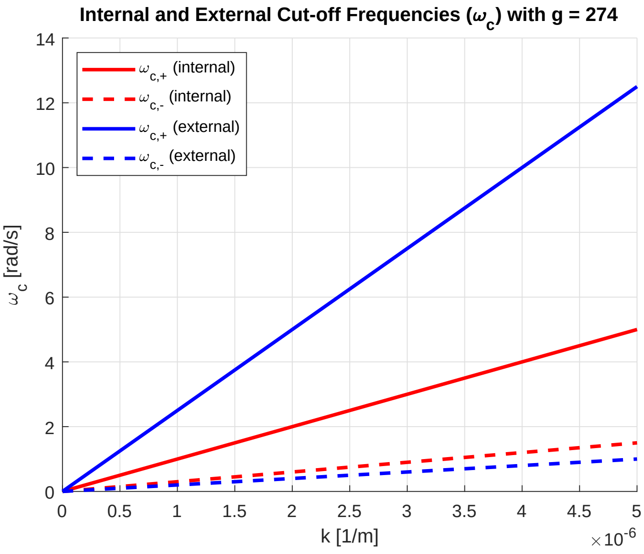

Figure 2: Cut-off frequencies ω_c as a function of the wavenumber k for $g = 274\ \mathrm{m\,s^{-2}}$. Solid curves represent $\omega_{c,+}$, while dashed curves correspond to $\omega_{c,-}$. Red curves show the internal plasma with $v_{Ai} = 1 \times 10^6\ \mathrm{m\,s^{-1}}$ and $c_{Si} = 3 \times 10^5\ \mathrm{m\,s^{-1}}$, and blue curves show the external plasma with $v_{Ae} = 2.5 \times 10^6\ \mathrm{m\,s^{-1}}$ and $c_{Se} = 2 \times 10^5\ \mathrm{m\,s^{-1}}$.

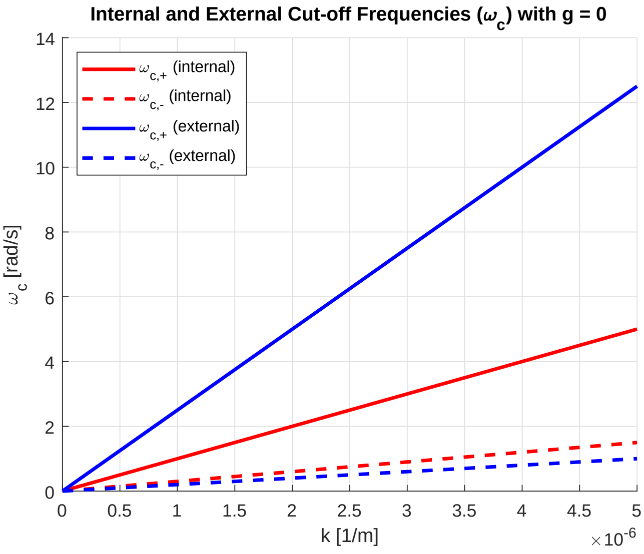

Figure 3: Cut-off frequencies ω_c as a function of the wavenumber k for $g = 0\ \mathrm{m\,s^{-2}}$. Solid curves correspond to $\omega_{c,+}$, and dashed curves represent $\omega_{c,-}$. Red curves indicate the internal plasma with $v_{Ai} = 1 \times 10^6\ \mathrm{m\,s^{-1}}$ and $c_{Si} = 3 \times 10^5\ \mathrm{m\,s^{-1}}$, while blue curves correspond to the external plasma with $v_{Ae} = 2.5 \times 10^6\ \mathrm{m\,s^{-1}}$ and $c_{Se} = 2 \times 10^5\ \mathrm{m\,s^{-1}}$.

The results show that the derived dispersion relation effectively captures the dependence of the phase speed on the density contrast and magnetic configuration, exhibiting distinct

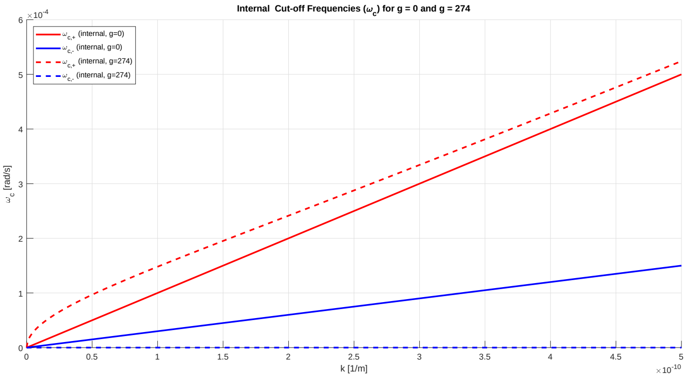

Figure 4: Comparison of internal cut-off frequencies ω_c for $g = 0$ (solid curves) and $g = 274$ m s^{-2} (dotted curves). Red curves correspond to $\omega_{c,+}$, and blue curves represent $\omega_{c,-}$.

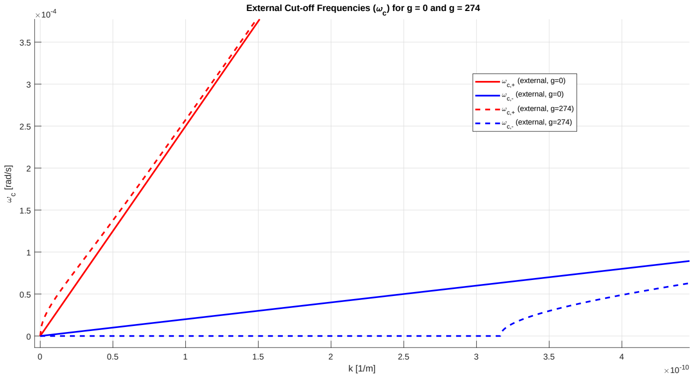

Figure 5: Comparison of external cut-off frequencies ω_c for $g = 0$ (solid curves) and $g = 274$ m s^{-2} (dotted curves). Red curves correspond to $\omega_{c,+}$, and blue curves represent $\omega_{c,-}$.

characteristics for sausage and kink modes. The inclusion of a constant gravitational acceleration introduces a small correction to the cut-off frequencies in the long-wavelength limit. As illustrated in Figs. 4 and 5, this correction becomes relevant only at very small values of k, where its contribution becomes comparable to the dominant restoring forces. Consequently, only a slight shift in the cut-off frequency appears for long wavelengths, whereas for short wavelengths (large k), the gravitational term rapidly becomes negligible, and the cut-off structure coincides with the gravity-free case. Moreover, increasing the external Alfvén speed relative to the internal sound speed tends to stabilize the loop against certain perturbations, while lower density contrasts enhance the relative importance of the gravitational correction in the long-wavelength regime.

Overall, these findings provide valuable analytical insights that complement numerical simulations and support the seismological diagnostics of solar coronal loops. The explicit demonstration of how a constant gravitational acceleration modifies the cut-off behavior—particularly in the long-wavelength limit—improves the physical interpretation of observed oscillatory signatures and enhances the usefulness of MHD waves as diagnostic tools in structured coronal plasmas.

Table 3: Physical parameters used for the dispersion relation [8].

Parameter	Value	Unit
External Alfvén speed (v_{Ae})	2500	$\mathrm{km\,s^{-1}}$
Internal Alfvén speed (v_{Ai})	1000	$\mathrm{km\,s^{-1}}$
External sound speed (c_{Se})	200	$\mathrm{km\,s^{-1}}$
Internal sound speed (c_{Si})	300	$\mathrm{km\,s^{-1}}$
Density ratio (ρ_e/ρ_i)	0.175	dimensionless

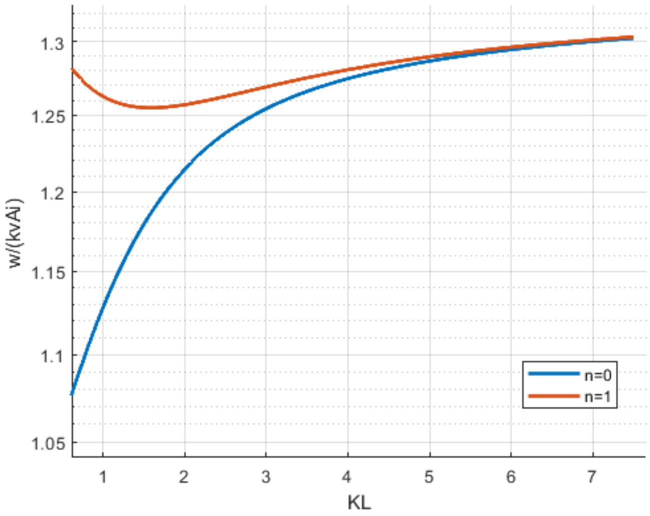

Figure 6: Normalized phase speed to internal Alfvén speed diagram versus kL for the dispersion relation without the incompressibility assumption and with gravitational acceleration, showing sausage ($n = 0$) and kink ($n = 1$) modes under hot coronal loop conditions.

4.1 Phase Speed Diagrams and Propagation Regimes

The horizontal axis of the phase speed diagrams represents the dimensionless parameter kL, defined as the product of the axial wavenumber k and the cylinder radius L. This parameter indicates the ratio of the cylinder's radial scale to the wavelength. In the diagrams of normalized phase speed c_{phase}/v_{Ai} as a function of kL, the wave behavior can be interpreted across distinct propagation regimes.

- **For $kL < 1$:** The cylinder acts as a thin waveguide. In this limit, wave propagation resembles one-dimensional behavior. The phase speed tends to specific characteristic values—such as the internal Alfvén or sound speed—indicating the dominance of long-wavelength effects.
- **For $kL \gg 1$:** The waves behave as high-frequency modes, and the influence of the radial boundary becomes less significant. In this regime, the phase speed tends to a

constant value or converges to an upper limit, reflecting the transition to wavelength-dominated propagation.

4.1.1 Behavior of Sausage and Kink Modes

As shown in Figs. 6 , the sausage and kink modes approach each other at particular values of kL, where their phase speeds act as asymptotes. This convergence behavior demonstrates a fundamental relationship between these two types of wave modes under varying waveguide thickness conditions.

4.2 Practical Applications of the Results

The results of this study have several important applications in solar and plasma physics. They can significantly improve the modeling of energy transport processes in the solar corona, particularly through a deeper understanding of magnetohydrodynamic (MHD) wave dynamics in coronal loops. Such insights are essential for exploring the mechanisms that may contribute to coronal heating.

A meaningful comparison with the classical work of Edwin and Roberts (1983) shows that the extended model developed here preserves the fundamental features of the classical dispersion relation while incorporating an additional physical ingredient—namely, the inclusion of a constant gravitational acceleration. This enables our model to reproduce the known gravity-free results in the appropriate limit, while also providing new analytical information on how gravity modifies the cut-off behaviour at long wavelengths. This constitutes a clear and defensible novelty beyond the 1983 model, which does not account for gravitational effects.

Furthermore, the analysis of wave behavior across different kL regimes and the observed convergence of phase speeds toward characteristic limits offer valuable information regarding mode stability. These results can be used to identify potential instability regions in magnetized structures and to guide seismological inversions aimed at constraining density contrasts, magnetic-field strengths, and the influence of gravitational forces in coronal loops.

Authors' Contributions

All authors have the same contribution.

Data Availability

No data available.

Conflicts of Interest

The authors declare that there is no conflict of interest.

Ethical Considerations

The authors have diligently addressed ethical concerns, such as informed consent, plagiarism, data fabrication, misconduct, falsification, double publication, redundancy, submission, and other related matters.

Funding

This research did not receive any grant from funding agencies in the public, commercial, or nonprofit sectors.

References

[1] Banerjee, D., Krishna Prasad, S., Pant, V., McLaughlin, J. A., Antolin, P., & et al. 2021, Space Science Reviews, 217.

[2] Pascoe, D. J., Nakariakov, V. M., & Arber, T. D. 2006, Astronomy and Astrophysics, 461, 1149.

[3] Nakariakov, V. M., Anfinogentov, S. A., Antolin, P., Jain, R., Kolotkov, D. Y., & et al. 2021, Space Science Reviews, 217.

[4] Gao, Y., Van Doorsselaere, T., Tian, H., Guo, M., & Karampelas, K. 2024, Astronomy and Astrophysics, 689, A195.

[5] Roberts, B. 1981, Solar Physics, 69, 27.

[6] Roberts, B. 1981, Solar Physics, 69, 39.

[7] Edwin, P. M., & Roberts, B. 1982, Solar Physics, 76, 239.

[8] Nakariakov, V. M., & Roberts, B. 1995, Solar Physics, 159, 213.

[9] Zsámberger, N. K., Allcock, M., & Erdélyi, R. 2018, Solar Physics, 853, 136.

[10] Edwin, P. M., & Roberts, B. 1983, Solar Physics, 88, 179.

[11] Parhi, S., De Bruyne, P., Murawski, K., & et al. 1996, Solar Physics, 167, 181.

[12] Priest, E. R. 2014, Solar Physics, 289, 3579.

[13] Reale, F. 2014, Living Reviews in Solar Physics, 11, 4.

[14] Bray, R. J., Cram, L. E., Durrant, C. J., & Loughhead, R. E. 2006, Plasma Loops in the Solar Corona. Cambridge University Press.